Desalination and Water Treatment
www.deswater.com
doi: 10.5004/dwt.2021.27336

228 (2021) 261–275
July

Use of alginate-chitosan/MWCNTs as a novel support for Ag_2O immobilization in catalytic reduction of 4-NP

Azeem Bibi[a], Sadiq-ur Rehman[a,*], Tasleem Akhtar[b], Kulsoom Akhter[a], Muhammad Imran Shahzad[c]

[a]*Department of Chemistry, University of Azad Jammu and Kashmir, Muzaffarabad, Pakistan, Tel. +92 3018086819; emails: srkhattak@gmail.com (Sadiq-ur-Rehman), azeembibi786@gmail.com (A. Bibi), kulsoom.chem@gmail.com (K. Akhtar)*
[b]*Department of Zoology, University of Azad Jammu and Kashmir, Muzaffarabad, Pakistan, email: seemeawan88@gmail.com*
[c]*Nano Sciences and Technology Department, National Center for Physics, 44000 Islamabad, Pakistan, email: Imran-shahzad@live.com*

Received 16 October 2020; Accepted 14 April 2021

ABSTRACT

This study contributes to the preliminary development of the industrial process in water purification, by introducing novel catalysts having immobilized silver oxide particles. For such a catalytic study, 4-NP was selected as a model sample. Synthesized catalysts Algi+Chito/multi-walled carbon nanotubes (MWCNTs), Ag_2O having SDS (Cs90 (Ag_2O)), Algi+Chito/MWCNTs, Ag_2O having CTAB (Cc90 (Ag_2O)), and Algi+Chito/MWCNTs, Ag_2O having DMF (CD90 (Ag_2O)) were comparatively characterized with respect to supporting matrices (Cs90, Cc90, and CD90 nanocomposites without silver oxide particles) by Fourier transform infrared, scanning electron microscopy, transmission electron microscopy, X-ray diffraction, Brunauer–Emmett–Teller, and mechanical testing. The catalysts have dispersed silver oxide particles, showed prominent peaks of participating components (Ag–O, COOH-MWCNTs, alginate, and chitosan), are more porous (surface area of (Cs90 (Ag_2O)), Cc90 (Ag_2O), CD90 (Ag_2O) is 8.671, 8.902, and 7.893 m^2/g, respectively), compact (swelling is 9.9, 9.1, and 7.2 g/g for Cs90 (Ag_2O), Cc90 (Ag_2O), CD90 (Ag_2O) catalyst), and mechanical strong (Youngs Modulus is 265.78 N/mm) than the supporting matrices. 4-NP was successfully catalyzed by synthesized catalysts in 20–60 min and followed the first-order kinetics in which the rate of reaction is accelerated by the amount of catalyst. Catalytically active nanocomposites could be reused at least five times with no mechanical loss, opening the possibility of recycling environmentally friendly catalysts in a continuous flow system. Surfactant-containing catalysts are more porous and liable for rapid catalytic reaction than non-surfactant-containing catalysts.

Keywords: Alginate-chitosan; Immobilization; Catalytic degradation; 4-NP; Silver oxide

1. Introduction

The development of nanotechnology provides unprecedented opportunities for scientific exploration in chemistry, physics, and engineering. In this context, metallic/metallic oxide particles particularly silver oxide nanoparticles have strikingly huge popularity owing to their unique properties like controlled size, various shape (diamond, octagonal, and thin sheets are common) surface plasma resonance in the visible region, nonlinear optical activity, and chemical stability [1]. These properties make the silver oxide particles as the most demanding in the field of water treatment, wound healing, drug delivery, catalysis, biosensing, and medical diagnosis [2,3].

However, the high surface activity, agglomerated behavior, and existence in colloidal form limit their applications

* Corresponding author.

in various fields, particularly in catalysis. This problem has been overcome by dispersing and immobilizing the nanoparticles in suitable support. The method of immobilization is a unique way in industrial catalysis due to greater recovery, recycling, reactive sites, and promising action (chemo and stereo-selectivity, stability, and diffusional action) [4]. Various materials like ceramics, glass beads, stainless steel, aluminum, metal alloys, and petroleum-based chemicals have been practiced as a supporting matrix for the immobilization of particles [5–12].

However, the current quest is for more clean, biodegradable, and sustainable materials that reduce the environmental impact due to their disposal after use [13,14]. The applications of natural polymers as a supporting matrix for immobilization of catalytic particles are believed as more efficient due to the large bonding potential for metal ions by complexation, chelation, and ion exchange mechanisms [14]. Moreover, the use of natural polymers as a supporting matrix not only reduces environmental pollution but also leads to sustainable production which decreases the implementation costs [15,16].

Among the various bio-based materials found naturally, alginate is becoming more competitive and accounts for a great number of industrial, medicinal, bakery, and food products. Alginate comprises of α-L-gluronic acid and β-D-mannuronic acid linked via β-1,4-glycosidic bonds [17]. The polymeric chain of alginate is flourished with plentiful OH and COOH groups. These groups are vulnerable to electrostatic interactions and H-bonding with other reactive substances and form jelly material. The type of jell formed by alginate polymer can be soft or hard that further depends upon the nature of crosslinking materials and crosslinking density [18].

Chitosan is another positive polysaccharide consist of glucosamine and acetyl-glucosamine units. The NH_3 and OH groups of these units have been exploited in various applications such as film-forming, metal ion sorption, drug delivery, and catalysis. However, it is known that these natural polymers are mechanically frail in their pristine form. To make them strong in a field like catalytic action, these natural polymers are crosslinked with suitable crosslinking material to use their wide range of applications in industry. For instance, Kamal et al. [19] reported the more strong and active form of chitosan in catalytic action by reacting the chitosan with CNTs. Similarly, another group of researchers demonstrated the more stable form of alginate by reacting the alginate with functionalized multi-walled carbon nanotubes (COOH-MWCNTs) [20,21]. Carbon nanotubes (CNTs) are the nanomaterials that act as the best reinforcing materials due to their high aspect ratio, surface area, chemical reactivity, and mechanical strength [22–24]. These particles potentially improved the thermo-mechanically performance as well as the surface area of the catalysts and provide the accessibility to coordinate the substrate molecules through a range of noncovalent bonding interactions [25]. A greater number of documents are filed in google in which CNTs-reinforcing materials of alginate and chitosan are formulated and showed promising properties.

Based on the importance of this work, attempts are made to formulate novel catalysts that would be more stable, porous, reactive, and eco-friendly. For such purpose, first, supporting matrices Cs90, Cc90, and CD90 nanocomposites were synthesized by a simple solution casting method without any crosslinking agent under ultrasonic waves. Then freshly prepared silver oxide nanoparticles were made to entrap and disperse uniformly in supporting matrices in the presence of sonic waves. These entrapped scaffolds (catalysts) were subjected to catalytic degradation of 4-NP to 4-AP in the presence of a reducing agent. The main objectives of the current study were to (i) introduce a new variety of catalysts having nanoparticles and natural supporting polymers; (ii) the role of surfactants in the catalytic action of catalysts; (iii) evaluate the effect of swelling and porosity on catalytic action of synthesized materials; (iv) assess the catalytic degradation of 4-NP in the presence of synthesized catalysts; and (v) examine the number of recycling turns in which prepared catalysts can efficiently perform catalytic actions and show encouraging results.

2. Experimental

2.1. Materials and methods

Sodium alginate (from brown algae, purity: 98%, CAS number: 9005-38-3, molecule weight: 405.2186 g/mol, 0.9 g), chitosan (purity: 99%, ≥75% deacetylated, CAS number: 9012-76-4, molecular weight: 20,000 g/mol, 0.18 g), 4-nitrophenol (4-NP), acetic acid, sodium dodecyl sulfate (SDS), cetyltrimethylammonium bromide (CTAB), dimethylformamide, sodium borohydride ($NaBH_4$), and silver nitrate ($AgNO_3$) were purchased from Sigma-Aldrich (UK) and used without further purification. COOH-MWCNTs (0.016 g) were kindly provided by the National Center for Physics (NCP), Pakistan. Deionized water was used throughout the procedure.

2.2. Synthesis of silver oxide nanoparticles

Metallic silver oxide nanoparticles were successfully synthesized by following a reported method [26]. In a typical procedure, an adequate quantity of $AgNO_3$ (170 mg) was stirred in distilled water to form a dilute solution (0.001 M). The other reagent $NaBH_4$ (0.378 mg) was separately dissolved in 500 mL of distilled water to form a 0.0020 M solution. Silver oxide particles were prepared by stirring the solution of $NaBH_4$ (ice-cold, 30 mL) by a cylindrical stirrer ("Cowie" 12 mm × 8 mm, 100–2,000 rpm) with $AgNO_3$ (10 mL, added dropwise, the time interval between two drops should at least 10 s) solution. The formation of silver oxide nanoparticles was indicated by the appearance of a yellowish-brown solution within 5 min. The solution mixture was filtered to obtain light brown precipitates of silver oxide, washed several times with distilled water, and dried in the oven at 150°C for 6 h. Prepared nanoparticles were sealed in vials and stored at room temperature for further use.

2.3. Synthesis of alginate-based matrices

Alginate-based supports for the immobilization of silver oxide particles were prepared by following a solution casting method under ultrasonic waves. Briefly, 0.9 g of sodium alginate was dissolved in 30 mL of D.I water by stirring at 40°C for 2 h. Chitosan (0.18 g) was separately dissolved in

acetic acid solution (2% (w/v), 75 mL) by stirring at 30°C for 1 h. COOH-MWCNTs (0.016 g) were uniformly dissolved in aqueous solutions (30 mL) having trace quantity of surfactants (SDS or CTAB) by ultrasonic waves produced by bath sonicator (Elmasonic S 30 H, 50–60 H). Alginate-based matrices (Cs90, Cc90, and CD90) were prepared by sonicating the mixture solution of alginate (2 mL), COOH-MWCNTs (2 mL), and chitosan (75 mL) for 5 h at 40°C. The obtained homogeneous mixture solution was poured into Petri plates and kept in a dust-free environment at room temperature for 3–4 weeks. Alginate-based nanocomposites films were washed with ethanol and dehydrated in the oven at 40°C for 5 h. Dried films were stored in sealed polyethylene bags for further processing.

The different supporting matrices were formulated and coded as Cs90 (having SDS surfactant), Cc90 (having CTAB surfactant, and CD90 (no surfactant is used and COOH-MWCNTs are dispersed in DMF).

2.4. Preparation of alginate-based catalysts

Matrix-supported catalysts (named as Cs90 (Ag_2O), Cc90 (Ag_2O), and CD90 (Ag_2O)) were prepared by solution blending methods under ultra-sonic waves. For such synthesis, freshly prepared silver oxide particles (0.09 g) were uniformly dispersed in blended mixtures of supporting matrices (Cs90, Cc90, and CD90) by sonic waves for 5 h at 40°C. The obtained viscous mixtures were poured into Petri plates and dried at room temperature for 3–4 weeks. Obtained catalysts (films) were washed several times with ethanol and dehydrated at 40°C for 5 h. Dried films were stored for further use.

2.5. Characterization techniques

Synthesized silver oxide nanoparticles, supporting matrices, and catalysts were characterized and investigated. UV-visible spectra of silver oxide nanoparticles were recorded on a UV visible spectrophotometer (UV-1601 SHIMADZU, KOREA) by using a quartz cell half-filled with an aqueous solution containing dispersed silver oxide particles (dispersed under ultrasonic waves). Fourier-transform infrared (FTIR) spectra were carried out by FTIR spectroscopy (Perkin Elmer spectrum 100 series spectrometer, KOREA) working in the range of 4,000–400 cm^{-1} at 2 mm/s rates. For transmission electron microscopy (TEM) measurement of silver oxide particle, a specific quantity of sample (1.0 μL) was dispersed in water and placed on a carbon-coated Cu-grid (200 mesh) and the solvent was allowed to evaporate at room temperature. After drying the TEM images were taken on a JEOL JEM 1200 EXII (Japan) instrument operated at 100.0 kV accelerating voltage. To image the supporting matrix and nanocomposite catalysts, a small amount of sample was suspended in ethanol, and measurement was recorded. The surface morphology of synthesized materials (5 mm × 5 mm × 0.12 mm) was observed by the SEM technique using Joel JSM-6510LV (Japan) instrument working at 20 kV. The images were obtained at 300,000× (maximum magnification power) and 2.3 nm (maximum resolving power). The porosity and surface area of matrix nanocomposites as well as of nanocomposite catalysts was determined by the Brunauer–Emmett–Teller (BET; Quantachrome Nova 2200 e, USA) technique using 0.045 g of the sample at 273 K. The shape, geometry, and pattern of arrangement in components were determined by X-ray diffraction (XRD) technique. The instrument used for such measurement was of JDX-3532 diffractometer working at the voltage of 20–40 kV**.** The X-rays used were of 1.5418 Å to diffract the films (1 cm × 1 cm × 0.12 mm) with a scanning range of 0°–160°. The tensile strength and percent elongation at break were measured by using Universal Testing Machine (100–500 KN) at room temperature. The strips of prepared nanocomposites (20.00 mm × 15.00 mm × 0.12 mm) were prepared and mounted to a separate grip for the measurement of the tensile property. The test speed was set at 1.0 mm/min. This testing machine can use the maximum force of 100 KN and works at temperature ranges from –70°C to 300°C.

2.6. Measurement of swelling capacity

The swelling capacity of supporting matrices and their immobilized catalysts was assessed by immersing the films (14 mg) in 100 mL solution from each of the distilled water, variable pH, and saline solutions. The pH of the solution was adjusted from 2 to 13 and various saline solutions (0.15 M) were prepared from each of KCl, $BiCl_3$, $CaCl_2$, and $FeCl_3$ salts. After passing the specific period of swelling, the dipped films were removed from immersing solvents and dried in several folds of filter paper. This immersion and removal of films in respective solutions take place for that time until an equilibrium swelling was obtained. The weight of swollen films was measured in digital weighing balance and recorded. Swelling capacity was calculated by using Eq. (1) [27]:

$$\text{Swelling}\left(\frac{\text{g}}{\text{g}}\right)=\frac{\left(W_s-W_d\right)}{W_d} \tag{1}$$

Here W_s and W_d are "swollen" and "dry" weights of films at time "*t*", respectively.

2.7. Catalytic analysis

The catalytic efficiency of synthesized materials was analyzed in the reduction reaction of 4-nitrophenol (4-NP) to 4-aminophenol (4-AP) in the presence of a reducing agent $NaBH_4$. For such conversion reaction, an aqueous solution of 4-NP (20 mL, 0.40 mM) was mixed with an aqueous solution of $NaBH_4$ (50 mL, 10 mM). The color of the solution changed from pale yellow to yellowish-green due to the formation of phenolate ions. A small amount of sample (0.02 g, small pieces of films) was added to the reaction mixture, and progress of reduction reaction was checked by taking absorption spectra with respect to time.

2.8. Kinetics of catalysis

To determine the time-dependent rate of reaction, experimental data of catalytic reaction was fitted in zero-order, first-order, and second-order reactions. The mathematical expressions used in these models are represented in

Eqs. (2)–(4), respectively [28]. The slopes obtained in plots between absorbance data and variable time give the values of rate constants (k_1, k_2, and k_3).

$$\left[A\right] = -k_1 t + \left[A_0\right] \tag{2}$$

$$\ln\frac{\left[A_t\right]}{\left[A_0\right]} = -k_2 t \tag{3}$$

$$\frac{1}{\left[A_t\right]} - \frac{1}{\left[A_0\right]} = k_3 t \tag{4}$$

where A_t stands for the absorbance at time t, and A_0 is the absorbance at time 0, k_1, k_2, and k_3 are the rate constants for zero, first, and second-order reactions, respectively.

3. Results and discussion

3.1. Characterization of nanoparticles

UV-vis-spectrophotometry is an important tool to determine the physical state and electronic distribution of metallic oxide particles. Fig. 1a indicates the obtained UV results of prepared silver oxide nanoparticles. The formation of silver oxide particles is generally identified by the appearance of λ_{max} in the visible region (400–440 nm) [29]. Results of the current study demonstrated that prepared brownish-black nanoparticles of silver oxide showed an absorption peak with λ_{max} at 410 nm. The absorption peak at 410 nm is attributed to surface plasmon resonance (SPR) created in particle surfaces during the interaction of light with the surface. This interaction generated oscillation in conduction electrons and visible light interacts with the

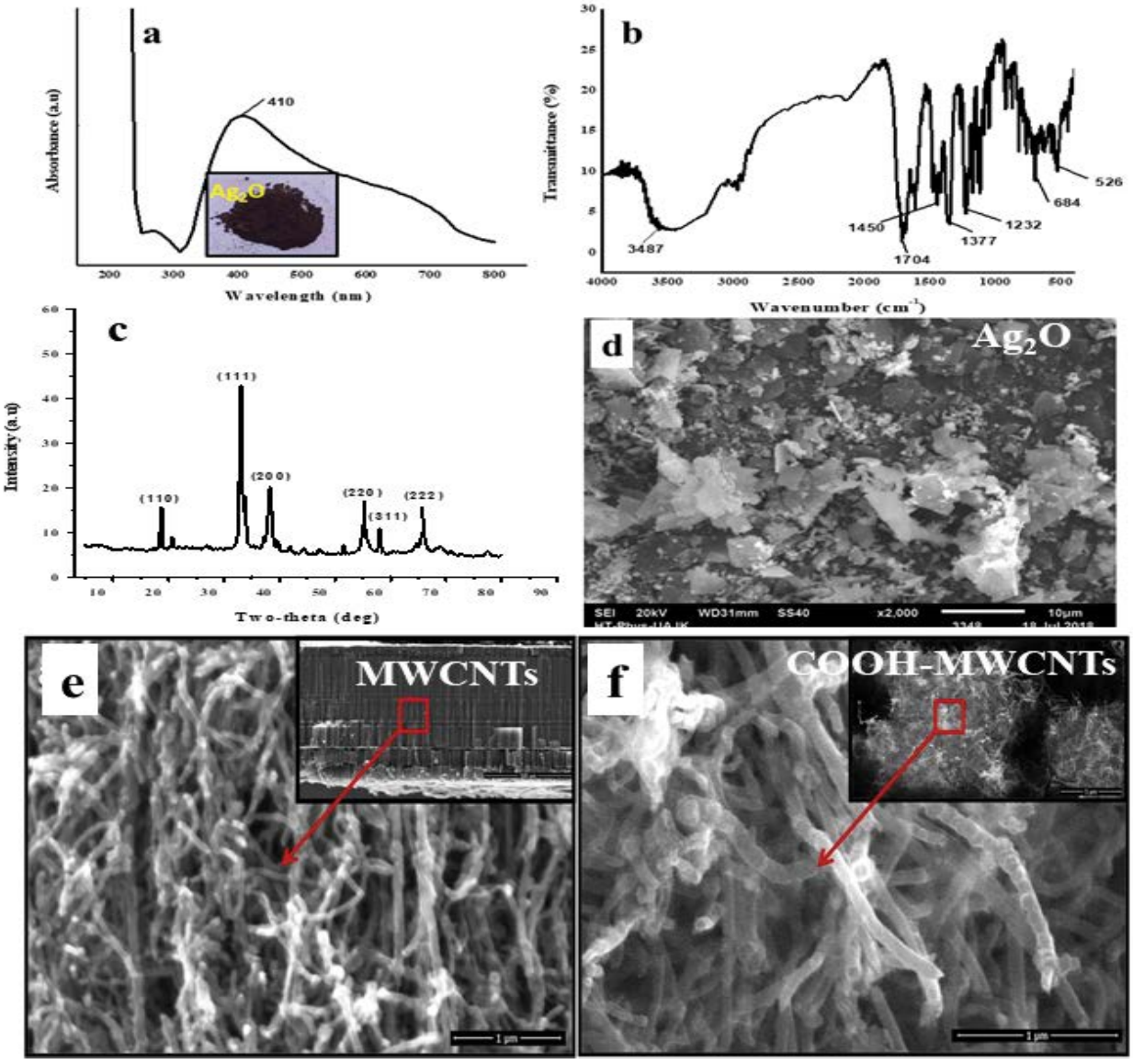

Fig. 1. (a) UV-vis, (b) FTIR, and (c) XRD results of Ag_2O, (d) SEM results of Ag_2O particles, (e) SEM results of as-grown CNTs in Carpet form, and (f) SEM results of functionalized-CNTs in powder form.

waves of oscillation, thus absorbed by the particles obtained in the form of λ_{max}. Silver oxide nanoparticles have unique optical properties, and their UV spectra provide a good deal related to the physical states of metallic oxides. According to Mie's theory, the shape of bands and the appearance of single or multiple bands indicate the size and geometry of particles. Spherical-shaped particles always give a single band whereas; non-spherical particles give two or three bands due to plasma resonances or quadrupole or higher multiple plasmon excitations [30]. The appearance of λ_{max} in the visible region and broad-shaped band of synthesized particles indicate bigger-sized particles with a larger diameter. Similarly, the formation of a slightly secondary band in as-grown particles is the sign of anisotropy present in particles. In anisotropic particles, quadrupole resonance is created on the surface of metallic oxide occurs in a different way than the primary dipole resonance. As a result, the un-evenly distribution of SPR occurs, which leads to shape-dependent SPR absorption spectra in non-spherical particles [31]. The obtained spectrum of as-grown silver oxide nanoparticles indicated that the particles are non-spherical in nature and have irregular geometry. The non-spherical shape of silver oxide particles is also indicated by SEM results.

The chemical structure of synthesized nanoparticles is characterized by FTIR spectroscopy. Fig. 1b indicates the important peaks obtained after FTIR characterization. The most prominent peaks obtained are at 3,487; 1,704; 1,450; 1,377; 1,232; 684; and at 526 cm^{-1}. The stretching vibration of the Ag–O bond appeared at 526 cm^{-1}, while the overtones produced by overlapping of stretching and bending vibrations give the absorption band at 684 cm^{-1}. The appearance of other absorption peaks present in the IR spectrum gives an indication of other materials in the form of impurities in the synthesized particles.

It is known from various studies that at the time of processing silver oxide particles at room temperature, the upper surface is tarnished by CO_2 and atmospheric oxygen (O_2). As a result of this chemical reaction, some molecules of silver oxide nanoparticles are converted into Ag_2CO_3. Due to the reaction of moisture (H_2O), these Ag_2CO_3 molecules are converted into complex basic silver carbonate, having the formula $AgOHAg_2CO_3$. The obtained IR peaks of synthesized nanoparticles lead us to conclude about the possibility of the formation of Ag_2CO_3 and complex $AgOHAg_2CO_3$ particles along with pure Ag_2O particles. The appearance of absorption peaks in the IR spectrum is in fact, the sign of υ_1, υ_2, υ_3, and υ_4 vibrations of carbonates and complex carbonates appeared at various energy bands [32,33]. The absorption peaks appeared at 3,478 and 1,704 cm^{-1}, respectively, are due to the stretching vibrations of the O–H and C=O group along with the presence of Ag–O groups appear at 3,478 and 1,704 cm^{-1}, respectively. Similarly, the appearance of a doublet at 1,450 and 1,377 cm^{-1} is, in fact, the confirmation of conversion to basic silver carbonate [33].

The structure and phase purity of synthesized silver oxide particles was analyzed by XRD analysis. Fig. 1c represents the XRD pattern of prepared nanoparticles. Diffraction peaks at 2θ = 32.95°, 38.30°, 55.18°, 65.64°, and 69.07° can be indexed as (111), (200), (220), (311), and (222), respectively, correspond to the cubic structure of silver oxide (Ag_2O) matched with standard JCPDS No. 00-001-1041. The shapes of peaks indicate that highly pure and crystalline silver oxide particles are prepared. There is an extra peak that appeared at the 2θ = 19.3°. This peak corresponds to the impurity (Ag_2CO_3) formed due to adsorbed moisture and CO_2 while annealing in air. This diffraction peak is indexed as (110) by matched with standard JCPDS No. 31-1236. The average crystallite size estimated with Scherrer's equation ($D = K\lambda/\beta\cos\Theta$, where D is the crystallite size, K is the shape factor, λ is the wavelength, β is the full width at half maximum (FWHM) and θ = diffraction angle) from most intense peak along (111) plan was 28.85 nm.

The formation of irregular-shaped, large-sized, and complex silver oxide particles along with pure silver oxide particles is also indicated by SEM analysis (Fig. 1d). SEM images declared that the prepared particles have irregular geometry, some of them are spherical in shape, while some are in different shapes. This difference in shapes is attributed to various oxidation states and the chemical composition of nanoparticles. The formation of carbonated and bi-carbonate silver oxide particles along with pure silver oxides give various shapes in SEM image. From the SEM image, it is also revealed that the prepared nanoparticles are not present in the agglomerated form, rather they exist in scattered form. The nature of dispersion is further increased by immobilizing the particles in the polymeric matrix.

The SEM micrographs of as-grown CNTs in Carpet form and functionalized CNTs in powder form are shown in Figs. 1e and f. The diameter of CNTs is in the range of 30–70 nm and the length is in micrometer range. In carpet form, the CNTs are vertically aligned and after acidic treatment, the powder has randomly oriented CNTs.

3.2. Characterization of supporting matrices and catalysts

Fig. 2a demonstrates the chemical structure of supporting matrices (Cs90, Cc90, and CD90) and immobilized catalyst (Cs90 (Ag_2O). Matrix materials that have a broad stretching band appeared at 3,600–3,000 cm^{-1} correspond to stretching vibrations of O–H bonds. Cs90 (Ag_2O) catalyst also showed the O–H stretching in the same region, indicating the persisting of hydroxyl groups in catalysts. This indication is also clarified by swelling capacity assessment (Fig. 4). Due to the involvement of metallic oxide particles, a lesser effect in hydrophilic domains was observed and catalysts showed slightly different swelling behavior compared to supporting materials. Conjugation of C=C bonds of MWCNTs is observed by stretching absorption appeared at 1,425 cm^{-1}. In catalyst, υ (C=C) shifted to a lower frequency (1,413 cm^{-1}) with lower intensity, suggesting the delocalization of π-electrons. Embedded silver oxide particles in the polymeric matrix may lead to electrostatic interaction between positive ended metallic center and electrons of C=C bonds, facilitates the relay of electrons between two ends, and eventually decreased the stretching frequency. The double-headed peaks of the N–H (amide group in chitosan) bond appeared in Cs90, Cc90, and CD90 are at 1,645 and 1,554 cm^{-1}. While these peaks are absent in catalysts. It is assumed that electropositive silver oxide particles are bonded with the N-atom of the N–H bond by intermolecular interactions. The high stability and leaching-less properties of immobilized metallic

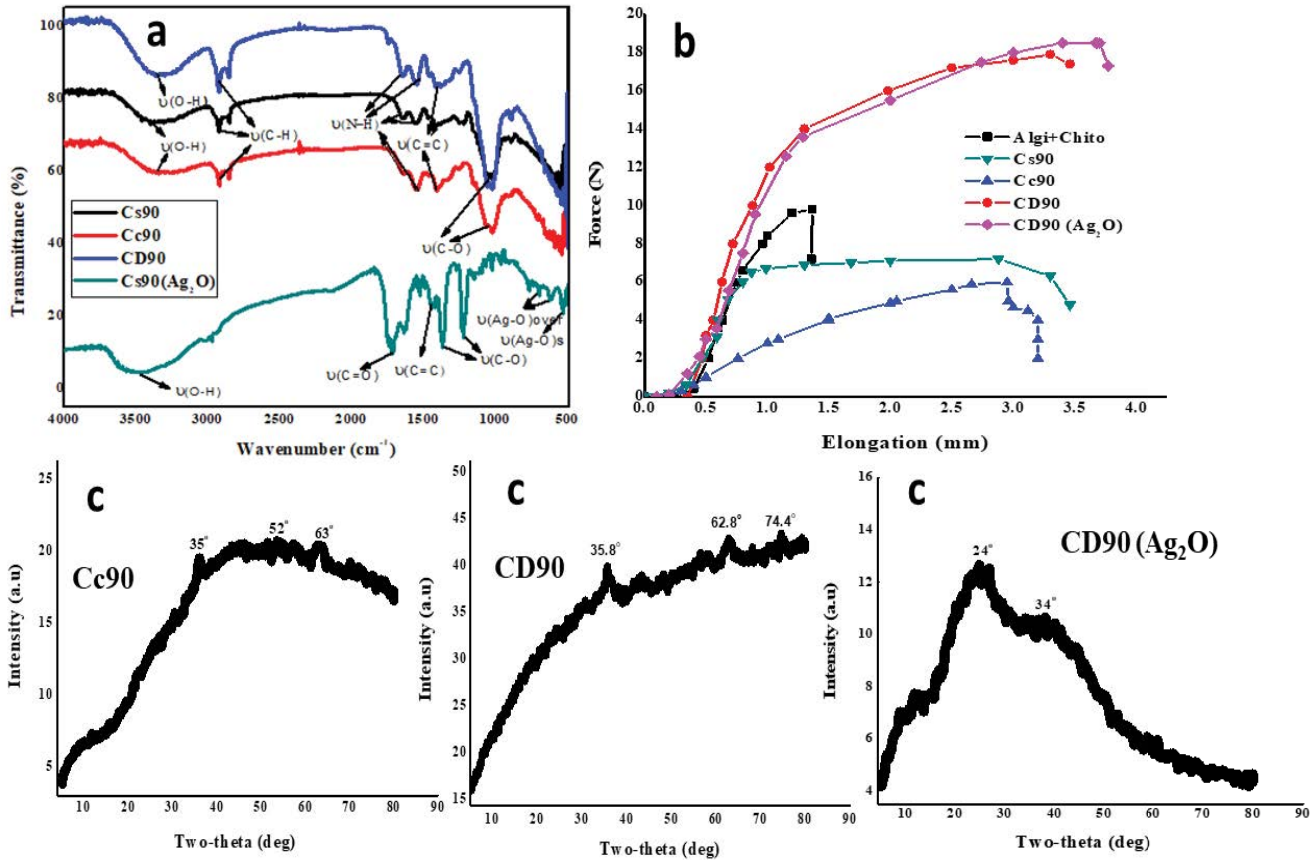

Fig. 2. Analysis of supporting matrices and catalysts by (a) FTIR, (b) Tensile testing, and (c) XRD measurement.

particles support the development of such types of electrostatic interactions. The presence of the Ag–O bond in the catalyst is indicated by stretching vibration that appeared at 528 cm^{-1}. Overtones produced by overlapping in stretching and bending vibrations of silver oxide particles are at 687, 684, and 679 cm^{-1}. The C–O bonds present in carbohydrate rings of supporting matrix and catalysts are indicated by stretching vibrations at 1,363 and 1,216 cm^{-1}. These results indicate that during fabricating the catalysts, the chemical composition and structure of materials remained intact and nanoparticles interact physiochemically with materials.

The catalysts should be strong enough to handle, wear, and use repeatedly in the reaction medium. We recorded the Youngs Modulus (N/mm), elongation at break (mm), stress at peak (N/mm), and strain at peak (%) of synthesized materials (Fig. 2b). Data from Table 1 indicates that Algi+Chito has poor mechanical integrity. So, their mechanical strength is improved by even the distribution of nanofillers under ultrasonic waves. The film of Algi+Chito showed Youngs Modulus 185.19 N/mm, while Cs90, Cc90, and CD90 matrices indicated its values in 129.55, 142.95, and 249.17 N/mm range. On the addition of silver oxide particles, values of Youngs Modulus increased (265.78 N/mm) in CD90 (Ag_2O) catalyst. In the same way, prominent improvement in elongation at break, stress at the peak, and strain at the peak were obtained after the addition of silver oxide nanoparticles in catalysts. The supporting materials Algi+chito and Cs90, Cc90, and CD90 break at 1.32, 3.28, 3.17, and 3.4 mm, respectively, while catalyst (CD90 (Ag_2O) break at 5.04 mm. Prepared catalysts also showed the highest strain at peak (17.05%) compared to supporting matrices Cs90 (3.82%), Cc90 (14.46%), and CD90 (15.83%). Similarly, the stress at the peak for the catalyst is greater (9.94 N/mm) than the supporting matrices (1.57, 3.21, and 9.84 N/mm) and also from the Algi+Chito complex (5.36 N/mm). On the comparative study of nanocomposites, having surfactants and without surfactants, it is noted that the nanocomposite films without surfactants (CD90) have a high value of tensile strength compared to films having surfactants (Cs90 and Cc90). The inclusion of surfactants in nanocomposites makes the materials porous due to micelles formation, thus stability reduced.

The blended scaffolds of catalysts are amorphous in nature with some degree of crystallinity that is indicated by the XRD results (Fig. 2c). These crystallites may develop due to proper arrangements produced in polymeric chains. The sorts of interactions between nanofillers and polymers reduced segmental motion and arrayed the chains. The presence of crystallites is indicated by the presence of some small peaks obtained at about $2\theta° = 35.6°$, 58.7°, and 62.7° in Cc90, $2\theta° = 35.8°$, 62.8°, and 74.4° in CD90, and $2\theta° = 24°$, 34° in CD90 (Ag_2O) catalyst. In the comparison of the peak pattern of nanocomposites with that of nanoparticles, the crystalline peaks of silver oxide disappeared in nanocomposite due to electrostatic interactions and H-bondings among alginate-chitosan, MWCNTs, and metallic oxide

Table 1
Values of tensile parameters obtained in mechanical testing

Types of films	Elongation at peak (mm)	Elongation at break (mm)	Load at peak (N)	Strain at peak (%)	Stress at peak (N/mm)	Youngs modulus (N/mm)
Algi+Chito	1.28	1.32	9.65	6.41	5.36	185.19
Cs90	0.764	3.28	2.84	3.82	1.57	129.55
Cc90	2.89	3.17	5.78	14.46	3.21	142.95
CD90	3.38	3.4	17.72	15.83	9.84	249.17
CD90 (Ag_2O)	4.78	5.04	19.78	17.05	9.94	265.78

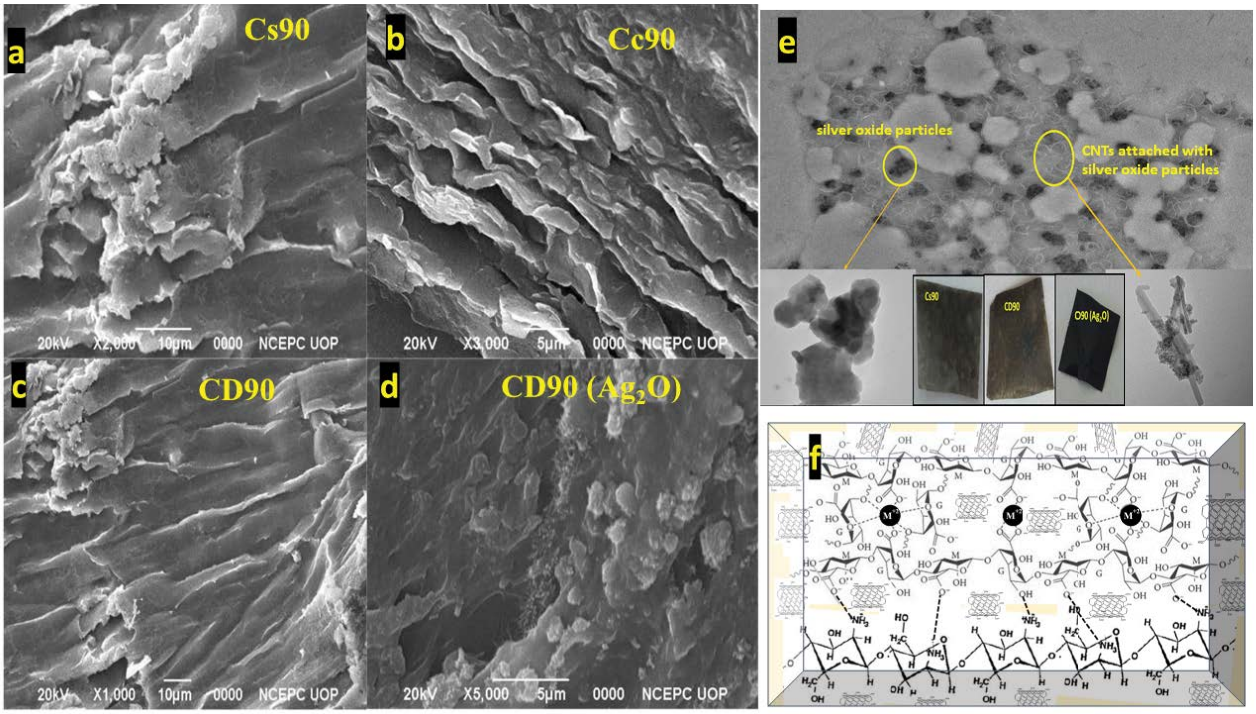

Fig. 3. (a–d) SEM images of supporting matrices and catalysts, (e) TEM image of CD90 (Ag_2O) catalyst, and (f) proposed structure of CD90 (Ag_2O) catalyst.

particles. The peaks obtained in nanocomposites are also less intense than silver oxide particles which are attributed to linkages present between components.

The surface texture of synthesized catalysts before and after the addition of silver oxide particles was visualized by SEM analysis and shown in Figs. 3a–d. It is indicated from images that metallic oxide particles are uniformly dispersed and attached in a complex matrix of polymeric structures. Alginate is a negative polysaccharide while chitosan is a positive one. On suitable contacting, both polysaccharides react with each other in the presence of sonic waves and nanofillers (COOH-MWCNTs). A strong polyelectrolytic complex is formed with plentiful reactive centers (OH, COOH, and NH_2 functional groups) and voids. On the addition of silver oxide particles in a polymeric matrix, reactive centers, and cavities entrapped these particles thus porous scaffolds (catalysts) are formulated. COOH-MWCNTs attached with polyelectrolytic complex provide a greater surface area to silver oxide particles by coordinating substrate molecules through noncovalent interactions. This dispersed nature of nanoparticles leads to the more stable, porous, and active form of catalysts. Bibi et al. reported that there is a direct relationship between catalytic action and porosity [14]. Our results related to cohesiveness by the incorporation of metallic particles are also in accordance with the reported data [14]. It is also obtained that during the catalyst's formulation under sonic waves, washing, and drying process, embedded nanoparticles remained intact and entangled form.

The dispersed and immobilized nature of silver oxide particles in the supporting matrix was confirmed by the TEM image. Fig. 3e reveals the physio-chemically attachment of silver oxide particles with COOH-MWCNTs and Algi+Chito complex. Pi-electrons (electrons of C=C, C=O bonds) of COOH-MWCNTs possibly interact with electropositive silver oxide particles and attached them to their surface. Moreover, the N–H, C=O, and C–O groups of the polyelectrolytic complex may bound with silver oxide particles and immobilized them. Such sorts of interactions have

Table 2
Surface area of synthesized supporting matrices and catalysts

Types of samples	Specific surface area (m^2/g)	Pore volume (cm^3/g)	Pore width (nm)
Cs90	8.436	0.047	3.179
Cc90	8.195	0.033	3.537
CD90	7.854	0.036	3.902
Cs90 (Ag_2O)	8.671	0.069	3.381
Cc90 (Ag_2O)	8.902	0.079	3.502
CD90 (Ag_2O)	7.893	0.056	3.997

also appeared in the FTIR spectrum of catalysts. TEM image also indicated that there are some particles of silver oxide which agglomerated and appeared in the form of the cluster in obtained results.

The surface area of synthesized catalysts was evaluated before and after the addition of silver oxide particles by the BET technique. Table 2 indicates that BET area of nanocomposite matrices (before the addition of silver oxide particles) is lesser (8.436, 8.195, and 7.854 m^2/g in Cs90, Cc90, and CD90) than the synthesized catalysts (8.671, 8.902, and 7.893 m^2/g in Cs90 (Ag_2O), Cc90 (Ag_2O), and CD90 (Ag_2O) catalyst, respectively). Similarly, the values of pore volume increased after the inclusion of silver oxide particles, and these values increased from 0.047, 0.033, and 0.036 cm^3/g (in Cs90, Cc90, and CD90) to 0.069, 0.079, and 0.056 cm^3/g (in Cs90 (Ag_2O), Cc90 (Ag_2O), and CD90 (Ag_2O catalyst, respectively). However, no regular pattern in pore width (nm) was obtained after the inclusion of metallic nanoparticles. It is obtained that the catalysts having surfactants (Cs90 (Ag_2O), Cc90 (Ag_2O),) are more porous in nature than the CD90 (Ag_2O) catalyst. This higher value may be due to the involvement of co-solutes in micelles formation around the positive metallic ions. The greater porosity provides a more favorable condition to enhanced catalytic reaction because of increased solvent diffusion [14]. Additionally, the greater surface area is also responsible to provide maximum reactive centers to the reaction medium [14]. The more porous nature of catalysts suggests applying the nanomaterials as the best catalysts for the reduction of 4-nitrophenol to 4-aminophenol.

3.3. Swelling measurement

Synthesized catalysts were evaluated by swelling capacity and compared with matrix nanocomposites (Cs90, Cc90, and CD90) (Figs. 4a and b). It is obtained that in aqueous media, the swelling tendency of Cs90 (Ag_2O), Cc90 (Ag_2O), and CD90 (Ag_2O) is lesser (9.9, 9.1, and 7.2 g/g) than their respective Cs90, Cc90, and CD90 (11.5, 10.89, and 7.63 g/g) nanocomposite. It is due to the reason that the presence of Ag_2O nanoparticles in the supporting matrix undergoes electrostatic force of attractions and H-bonding between COOH-MWCNTs, COOH, OH, and NH_3 groups and reduced the swelling capability. The possible forces of attraction between silver oxide particles and supporting matrix are shown by Fig. 3f. Lesser value of swelling in catalysts also leads us to conclude the utilization of hydrophilic domains (COOH, OH, and NH_3 groups) with nanoparticles, decreased segmental motion and convoluted/compact structures of catalysts are formulated compared to supporting matrices. Pasparakis and Bouropoulos [34] also indicated the reduced swelling of alginate polymer due to the crosslinking materials.

Figs. 4c and d represent the swelling capacity measurement at variable pH from pH 2 to 13. It is known that all the prepared catalysts including their supporting matrices showed similar behavior at variable pH, that is, it is lesser in acidic and basic pH and greater in neutral pH. Cs90 (Ag_2O), Cc90 (Ag_2O), and CD90 (Ag_2O) catalyst showed 5.6, 4.6, and 3.2 g/g in acidic, 2.5, 3.2, and 2.1 g/g in basic and 8.6, 8, and 7.8 in neutral pH while the matrices Cs90, Cc90, and CD90 showed 7.6, 5.6, and 6.2 g/g in acidic 1.3, 1.2, and 1.8 g/g in basic and 11.3, 8.9, and 7.8 g/g in neutral pH. In acidic pH protonation of COOH, NH_3, and OH groups and screening effect of counterions in basic pH squeeze the polymeric chains and lead to decreased swelling. While in neutral pH, deprotonation of COO^- ions and non-perfect anion-anion (COO^-) repulsion caused the polymeric chains to expand and swelling capacity increased [17].

The swelling behavior of synthesized catalysts was also comparably assessed with respect to supporting matrices in various saline solutions of KCl, $CaCl_2{\cdot}2H_2O$, $FeCl_3{\cdot}6H_2O$, and $BiCl_3$. Figs. 4e and f indicate that various charge densities of external solutions did not significantly screen the functional groups of catalysts in comparison with supporting matrices. It means, in catalysts due to the inherent crosslinking of silver oxide particles with functional groups of nanocomposite matrix, no free reactive moieties are available for further reaction with saline ions. The effect of Ca^{2+} (divalent) ion to react with polymeric chains is greater (least swelling) than K^{1+} (monovalent) and Fe^{3+}, Bi^{3+} (trivalent ions). This unique behavior of divalent ions is attributed to the formation of the egg-box model in the alginate-chitosan framework [35].

3.4. Catalytic action of synthesized materials in the reduction of 4-NP

Synthesized catalysts were applied for the catalytic reduction of 4-NP to 4-AP and results are shown in Figs. 5a–c. Practically, first of all, phenolate ions (greenish-yellow color) of 4-NP were produced by mixing the aqueous solution of $NaBH_4$ (50 mL, 10 mM) with 4-NP (20 mL, 0.40 mM). After that, an adequate quantity (0.04 g) of the prepared sample was added and stirred until the reaction reached equilibrium. The progress of the reaction was monitored by taking UV absorbance after time intervals. It is obtained from the experimental data that all the three prepared catalysts showed catalytic action for conversion of 4-NP to 4-AP in different time periods.

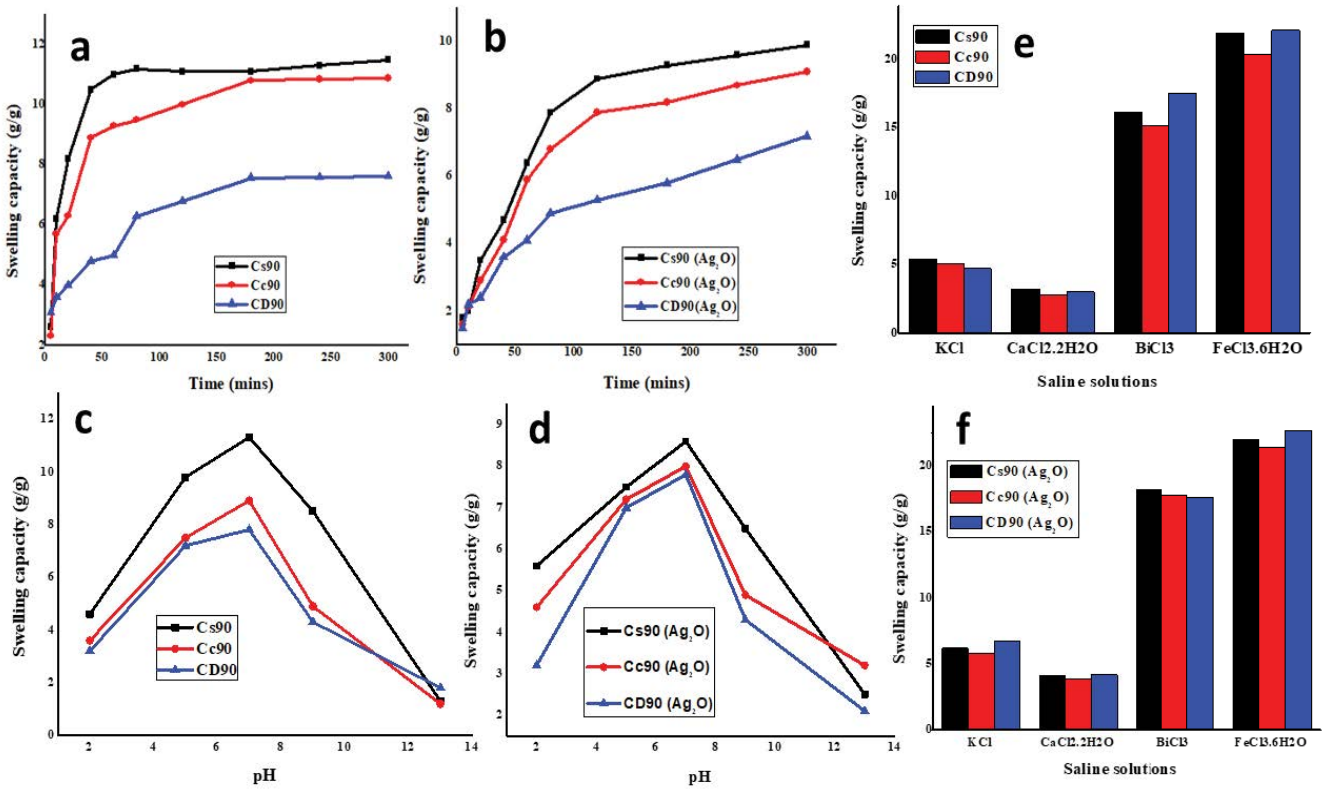

Fig. 4. Swelling behavior of supporting matrices and catalysts in (a and b) distilled water, (c and d) variable pH, and (e and f) various saline solutions.

Reported literature indicates that, in the presence of $NaBH_4$, the reduction reaction of 4-NP into 4-AP is thermodynamically favorable (E_0 for 4-NP/4-AP = –0.76 V and H_3BO_3/BH_4^- = –1.33 V vs. NHE), but the large potential difference between the donor ($NaBH_4$) and acceptor (4-NP) creates a kinetic barrier for the feasibility of this reaction [28]. Prepared catalysts possibly decreased this barrier, and the flow of electrons takes place from BH_4^- to 4-NP. This catalytic conversion was confirmed by UV absorption spectra. The UV spectra indicated that 4-NP absorbed UV light at about 317 nm before the addition of reducing agents and catalysts. When $NaBH_4$ was added, the UV absorption band at 317 nm disappeared and a new redshift at 400 nm appeared. This absorption at the visible region corresponds to nitrophenolate ions of 4-NP. On the addition of a small piece of catalyst, there is a rapid decrease in intensity of absorption spectra at 400 nm, while there is a concomitant increase in the absorption spectra of a new peak at 260 nm. The absorption peak at 260 nm is in fact, the confirmation of preparation of 4-AP. The formation of 4-AP is also indicated by a change in color from yellowish-green to an almost colorless solution (Fig. 5d). The decreasing intensity of λ_{max} at 400 nm indicated that Cs90 (Ag_2O) and Cc90 (Ag_2O) catalysts required 30 min for complete conversion of 4-NP to 4-Ap, whereas 60 min are needed to CD90 (Ag_2O) catalyst for this degradation reaction. In this process, both acceptor and donor molecules co-adsorbed at the surface of catalysts, and the relay of electrons takes place between two components that accelerate the reaction. In a study of a similar type, Gangula et al. reported the conversion of 4-NP to 4-AP in the presence of silver oxide particles. This catalytic reaction was investigated to complete within the time limit of 10–20 min which coincides with our results. The efficient activity of synthesized catalysts is the immobilization of silver oxide particles in supporting matrices. Algi+Chito/MWCNTs form a strong and porous polyelectrolytic complex that dispersed and bind silver oxide particles uniformly. The porous nature of the supporting matrix diffuses the solvent into the polymeric framework and facilitates the reaction to speed up by making metallic oxide centers more approachable [36–38]. Significantly no catalytic action was obtained, when supporting matrices (Cs90, Cc90, and CD90) were practiced putting in the reaction medium. From these results, it is concluded that the catalytic action of prepared catalysts is due to the presence of silver oxide particles. Synthesized catalysts were also comparatively analyzed for the catalytic action of 4-NP to 4-AP. It was investigated that the catalysts having surfactants (SDS and CTAB) showed efficient action in minimum time, while the catalyst CD90 (Ag_2O) (without surfactant) showed the reduction reaction in delayed time. The more rapid action of Cs90 (Ag_2O) and Cc90 (Ag_2O) catalysts in the conversion of 4-NP to 4-AP is due to the involvement of surface-acting agents. These surfactants act as a capping agent for metallic particles and facilitate dispersion [39]. Highly dispersed metallic oxide particles have greater reaction sites for catalytic action; hence the rate of reaction is increased. Additionally, due to being water-soluble, surfactants increase the influx of aqueous solution of 4-NP into voids and cavities of catalysts, which lead to the

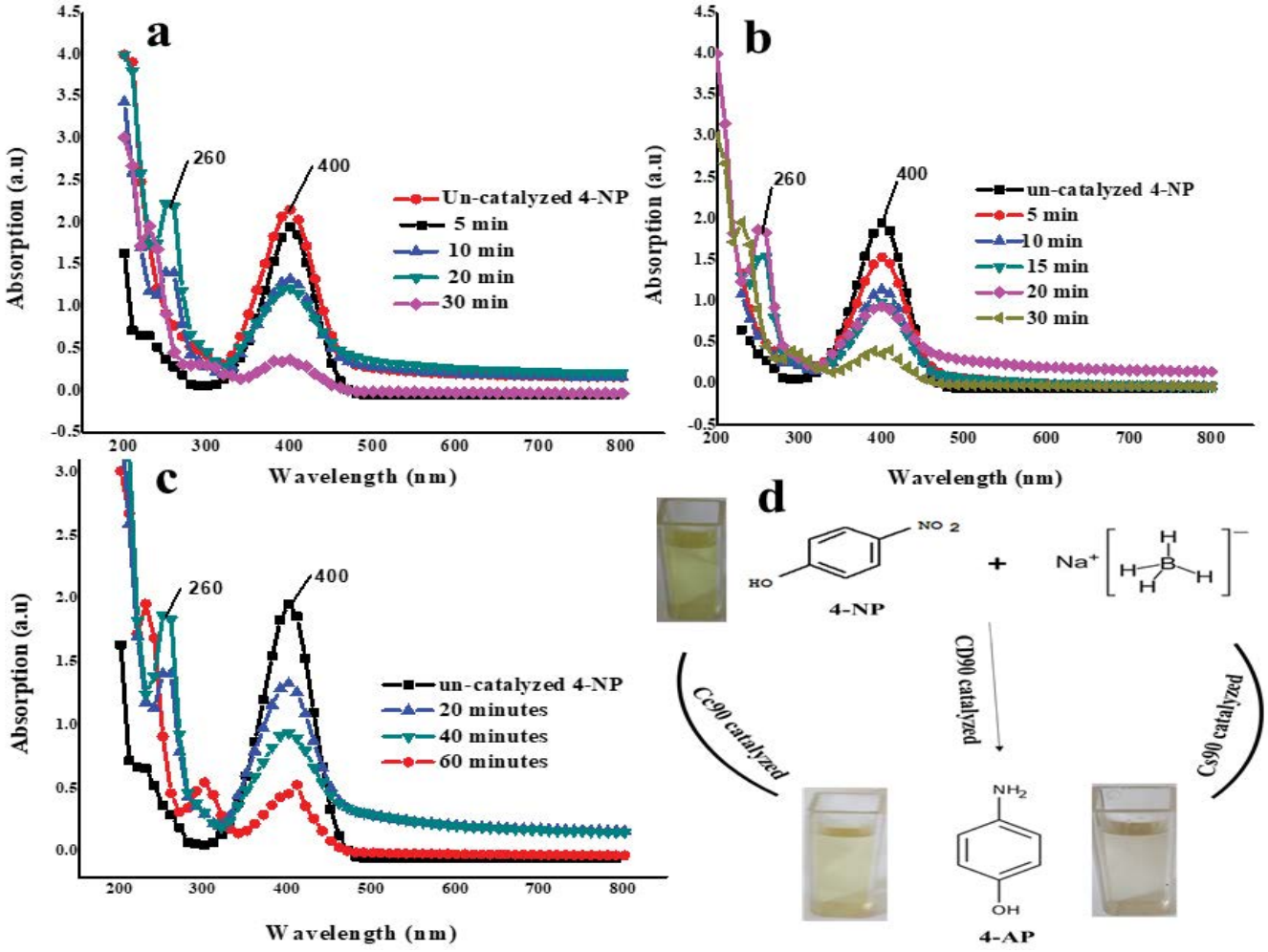

Fig. 5. UV results of conversion of 4-NP to 4-Ap in the presence of (a) Cs90 (Ag_2O) catalyst, (b) Cc90 (Ag_2O) catalyst, (c) CD90 (Ag_2O) catalyst, and (d) reaction pathways and colors obtained for conversion of 4-NP to 4-AP in the presence of synthesized catalysts.

rapid catalytic action. However, in a catalyst having no surfactant (CD90 (Ag_2O)) delayed time (60 min) was required to penetrate the solvent in the framework of the polymeric matrix and reach to reactive sites of catalysts. As a result, prolonged time was required to convert the 4-NP to 4-AP in the presence of the CD90 (Ag_2O) catalyst.

The change in concentration of 4-NP with respect to time after the application of catalysts is represented by Fig. 7d. Results demonstrated the more steepness for the plots of concentration degraded in the presence of surfactants-containing catalysts than the CD90 (Ag_2O) catalyst. This indicated the greater amount of 4-NP reduced at each step by Cs90 (Ag_2O) and Cc90 (Ag_2O) catalysts than by CD90 (Ag_2O) catalyst.

3.5. Kinetics of catalytic action

The kinetics of catalytic action was studied by applying zero-order, first-order, and second-order kinetic models. The values of correlation coefficients and rate constants included in Table 3 (obtained by slopes) are used to investigate the most suitability of the respective model in the degradation reaction of 4-NP. Figs. 6a–c indicate the difference in slopes obtained after applying three models in which A_t/A_0 vs. time was plotted. Values of rate constants indicated that the greater values of "k" are obtained in the first-order kinetic model in comparison with zero and second-order ones. Moreover, R^2 values are close to unity (R^2 values are 0.987, 0.987, and 0.968 for Cs90 (Ag_2O), Cc90 (Ag_2O), and CD90 (Ag_2O) catalysts, respectively) in the first-order model whereas, its values are less than unity in zero-order and second-order kinetic model. These results indicate that in the catalytic reduction of 4-NP to 4-AP, the first-order reaction was followed in which the rate of reaction is proportional to the concentration of one reactant. The limiting reactant in this reaction is possibly the concentration of the catalyst. As the concentration of catalysts increased, the number of reacting cites also increased which led to a greater number of molecules of 4-NP degraded. The obtained results coincide with other studies of the reduction of 4-NP in the presence of other catalysts [40,41]. After a comparative analysis of various synthesized catalysts, the rate of reactions of Cs90 (Ag_2O) and Cc90 (Ag_2O) catalysts is greater with greater rate constants (6.5×10^{-2} and 6.6×10^{-2},

Table 3
K, *T*, and R^2 values obtained after applying zero, first, and second-order kinetic models

S. No	Catalysts	R^2	$K \times 10^{-2}$ min^{-1}	Time for completion (min)
1	Zero-order kinetics			
	Cs90 (Ag_2O)	0.9825	7.58	30
	Cc90 (Ag_2O)	0.928	5.66	30
	CD90 (Ag_2O)	0.8665	2.76	60
2	First-order kinetics			
	Cs90 (Ag_2O)	0.987	6.5	30
	Cc90 (Ag_2O)	0.987	6.6	30
	CD90 (Ag_2O)	0.968	5.6	60
3	Second-order kinetics			
	Cs90 (Ag_2O)	0.884	1.1	30
	Cc90 (Ag_2O)	0.751	3.6	30
	CD90 (Ag_2O)	0.922	3.2	60

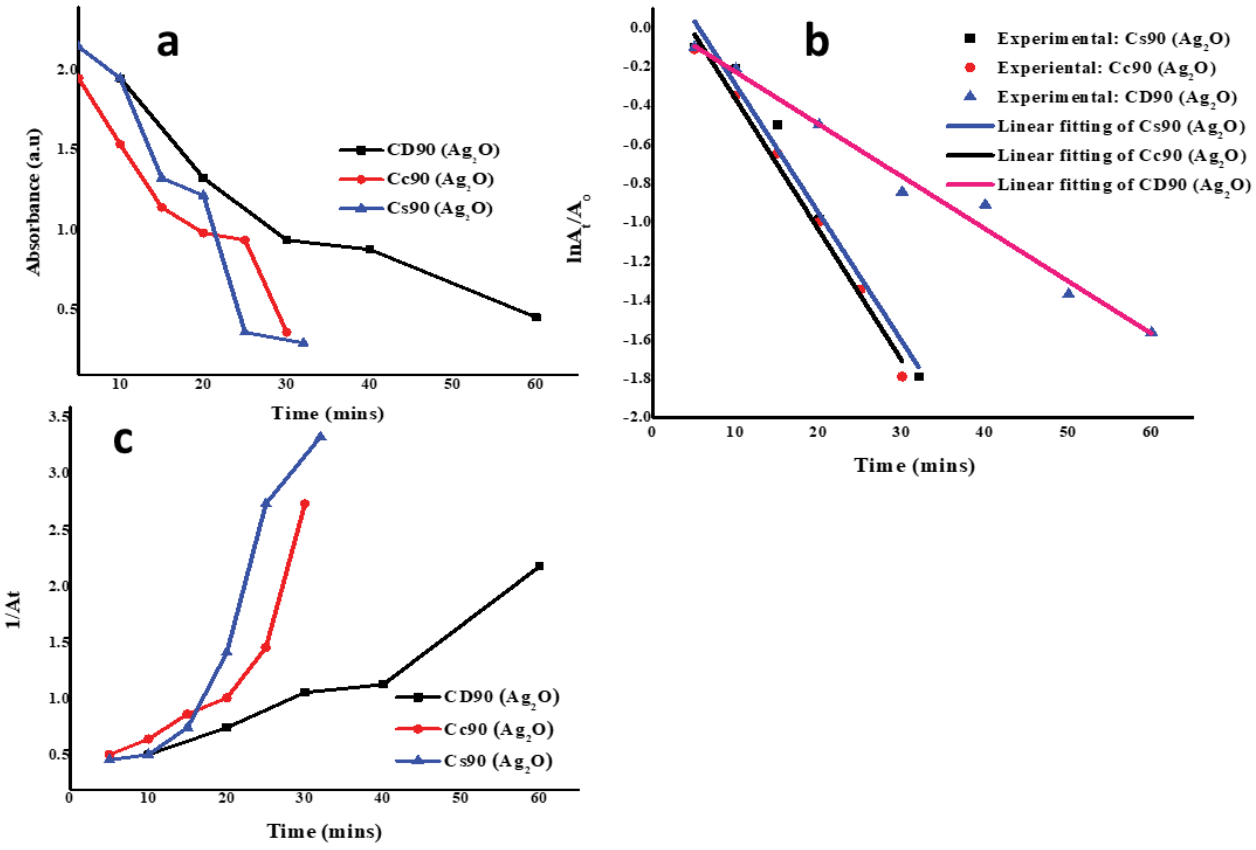

Fig. 6. Time-dependent plots were obtained after applying (a) zero-order, (b) first-order, and (c) second-order kinetics on catalytic reduction of 4-NP to 4-AP.

respectively) than the catalyst having no surfactant (CD90 (Ag_2O) (5.6×10^{-2}). SDS and CTAB surfactants possibly react and surround the positively charged silver oxide ions by micelle formation. On immersing in the reaction medium, the influx of reactants may cause the dissolution of these micelles, result in the exposure of metallic oxide reactive centers to reactants. On the other hand, in CD90 (Ag_2O) catalyst, the decrease in *k*-values occurred due to the coverage of metallic oxide centers by the bulk of biomolecules. Such polymeric coverage retards the diffusion of 4-NP to the catalytic surface and resultant slowdowns the reaction. Gangula et al. [28] and Esumi et al. [42] showed similar results in decrease the catalytic reduction of 4-NP due to biomolecular coverage of catalytic centers.

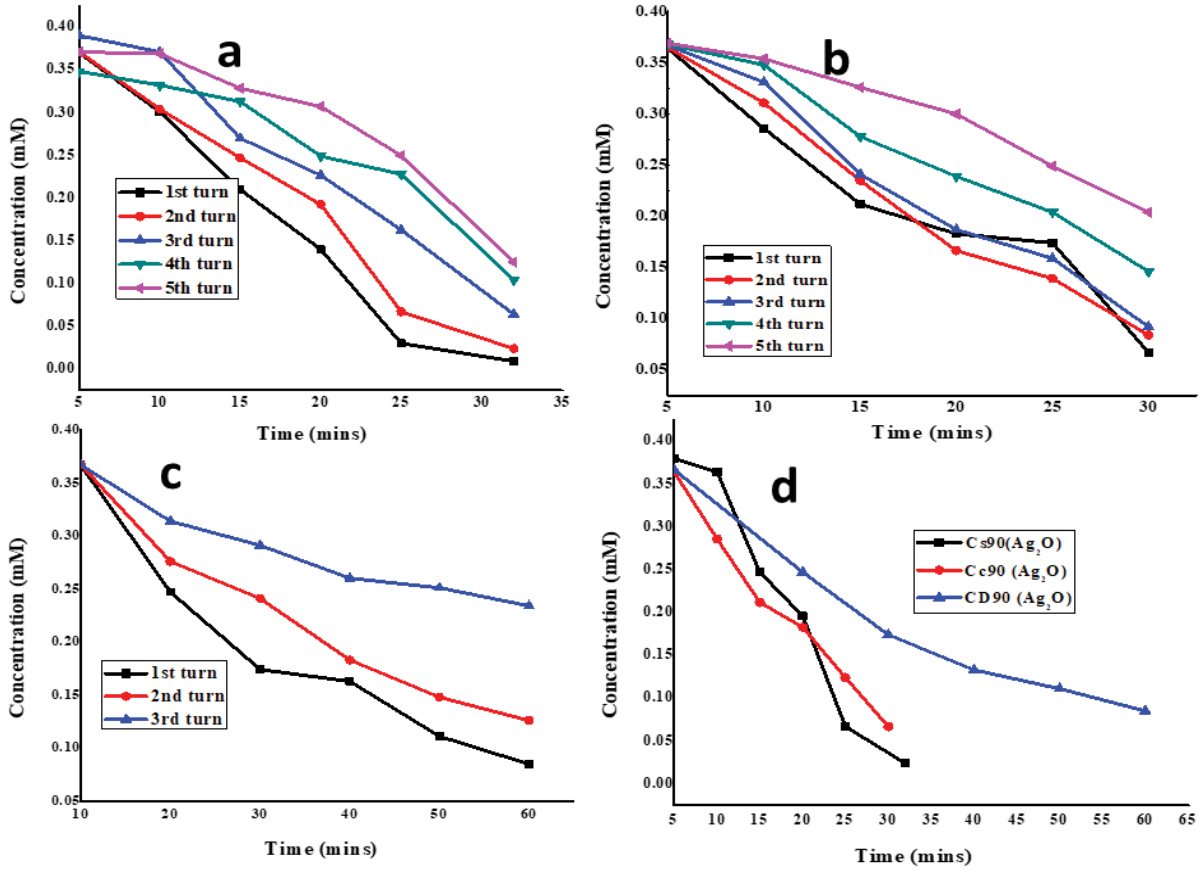

Fig. 7. Comparative plots of change in concentration of 4-NP in recycling turns in the presence of (a) Cs90 (Ag_2O) catalyst, (b) Cc90 (Ag_2O) catalyst, (c) CD90 (Ag_2O) catalyst, and (d) the presence of synthesized catalysts.

3.6. Recycling of catalysts in the reduction reaction of 4-NP to 4-AP

To evaluate the possibility of recycling of synthesized catalysts for continued use in the reduction of 4-NP, experiments were carried out many times. For this performance, the catalyst used for each process was washed (3–4 times) with distilled water and used for the next experiment. Figs. 7a–c indicated the change in concentration of 4-NP in various turns of recycling in the presence of various catalysts. In each turn of recycling, the concentration of 4-NP is decreased, and it became a minimum at the last regenerating time. The minimum concentration of 4-NP degraded is indicated by the less steepness of the graph. Results also indicated that, at each repeated time, the amount of 4-NP degraded by Cc90 (Ag_2O) and Cs90 (Ag_2O) catalysts are greater than by CD90 (Ag_2O). Moreover, a surfactant containing catalysts degraded the maximum concentration in lesser time units.

The kinetic behavior of catalytic reduction of 4-NP in each recycling time is included in Fig. 8. It is known that an improvement in the catalytic reaction was obtained in recycling reactions of 4-NP, as an increase in A_t/A_0 was obtained on increasing the recycling turn. A possible reason is that in the first use the reactant is not completely penetrated in the framework of the catalyst. In repeated use of experiments, due to greater swelling and segmental motion (as the optimum time for maximum swelling is about 300 min) molecular structure expands and greater the number of molecules have the ability to reach the reactive centers. However, after the use of 5th times in (Cs90 (Ag_2O) and Cc90 (Ag_2O) catalysts and 3rd time in CD90 (Ag_2O) catalyst, the degradation reaction slows down. This decreased efficiency may be attributed to the saturation of reactive centers of catalysts by 4-NP and further reaction medium do not affect largely.

In the field of catalysis, the recovery of catalysts is a big issue. Mostly, the catalysts employed in chemical reactions are converted into colloidal form due to the abrasion phenomena and are recovered by the centrifugation process, which is a difficult and costly task [43]. To avoid such a difficult job, the use of a supporting matrix to stabilize the catalysts is a growing trend. The supporting matrix not only immobilized the catalyst for providing large reactive centers but also minimize the leaching problem [14]. Therefore, we synthesized the immobilized catalysts in the bio-sources matrix and found the best results in the reduction reaction of 4-NP. The superior efficiency of synthesized catalysts is that after the use of recycling turns the abrasion phenomenon does not occur, which gives the sign of more stability and strong interactions in the framework of catalysts. Additionally, the synthesized catalysts have the potential to catalyze the reaction many times. After the application of such repeated times, the saturated centers

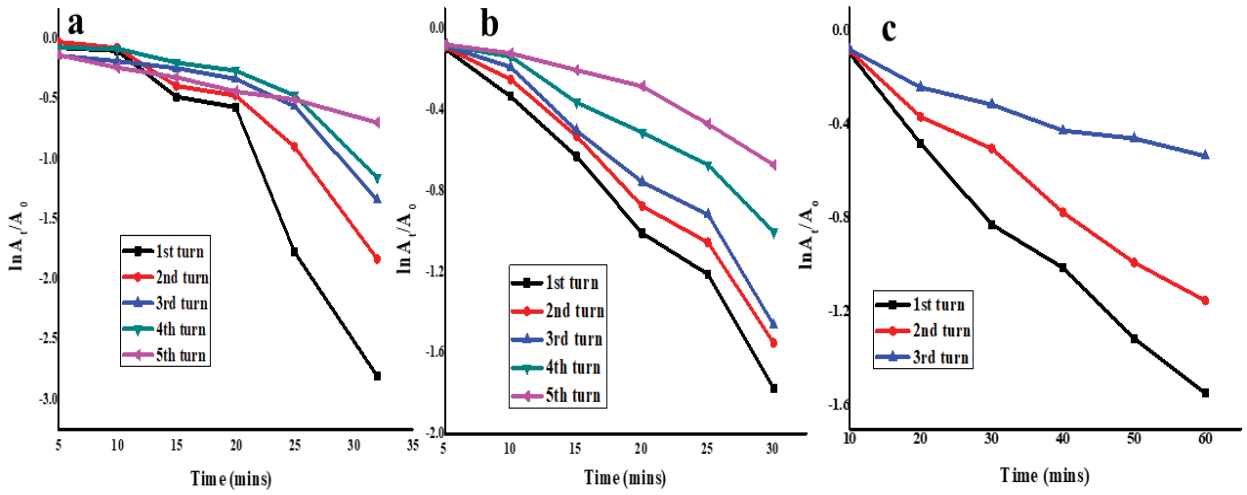

Fig. 8. Linear fitting of first-order kinetics on recycling turns for the conversion of 4-NP to 4-AP in the presence of (a) Cs90 (Ag_2O) catalyst, (b) Cc90 (Ag_2O) catalyst, and (c) CD90 (Ag_2O) catalyst.

Table 4
Comparison of catalytic degradation of synthesized catalysts with the reported catalysts

S. No	Catalysts	Reaction time (min)	Recycling turns	Rate constant	References
1	Alginate gel crosslinked with Ba^{+2} and Ag^{+1} ion	11	3	0.243 min^{-1}	[44]
2	Ag^{+1} ion embedded in Tapioca starch	15	1		[45]
3	Ag NPs-chitosan TiO_2	120	5	0.042 min^{-1}	[46]
4	Cl-CuO/g-C_3N_4	100	5	2.74×10^{-2} min^{-1}	[47]
5	Calcium Alginate-stabilized Au NPs	45	3	0.14×10^{-5} min^{-1}	[48]
6	Chitosan-Guar gum blend AgNPs	3	3	7.59×10^{-3} s^{-1}	[49]
7	Bentonite clay supported Fe NPs	20	5	0.1409 min^{-1}	[50]
8	Chitosan embedded Au and CNTs	3	10	0.021 s^{-1}	[11]
9	Ag NPs embedded in Algi+Chito/MWCNTs composite	30	5	$6.5–6.6 \times 10^{-2}$ min^{-1}	This work

of stable catalysts can be regenerated by physical (washed under sonic waves, microwaves, or stirring) or chemical processing (acid, base, or other reagent treatment to remove the adsorbed species) which needs further consideration. The prepared catalysts have the potential to employ in a filter-bed or in the lining of the reactor and are appropriate to use in a flow system. Moreover, these catalysts would be efficient for an extended period and recovery problems would be negligible.

3.7. Comparison with other studies

The comparative study of synthesized catalysts in degradation reaction of 4-NP was done with other matrix-embedded catalysts [14,44–50] listed in Table 4. The proposed porous nanostructures of synthesized catalysts are comparable and competitive with other ones. The efficient catalytic action and repeated regenerative cycles make the synthesized catalysts as most promising from a cost-effectiveness point of view. Other matrix-supported catalysts also showed the best and efficient action in the degradation reaction of 4-NP to 4-AP, but the synthesized Cs90 (Ag_2O), Cc90 (Ag_2O), and CD90 (Ag_2O) catalysts showed remarkable properties due to the presence of natural-based polymers. The eco-friendly and biodegradable nature of synthesized catalysts makes them as most demanding catalysts. Additionally, Cs90 (Ag_2O), Cc90 (Ag_2O), and CD90 (Ag_2O) catalysts degraded the 4-NP more than one time (5 times) due to greater mechanical strength and presence of reactive centers. The presence of surfactants and the dispersed nature of silver oxide particles in Algi+Chito/MWCNTs porous matrix provides the greater possibility to interact and catalyzed the reaction. Moreover, the greater surface area, nano-sized reinforcing particles, and dispersed nature of nanoparticles make the synthesized materials as more porous, stable, and efficient catalysts. The molecules of 4-NP adsorb on the surface of catalysts and degrade them into smaller less-toxic molecules.

4. Conclusion

- Alginate-based catalysts (Cs90 (Ag_2O), Cc90 (Ag_2O), and CD90 (Ag_2O) were successfully prepared by solution casting method under ultrasonic waves.

- The prepared catalysts showed the best thermomechanical strength, cohesiveness, dispersed metallic oxide particles, reactive sites, and immobilized nature indicated by characterization techniques.
- The 4-NP is a model pollutant that was successfully degraded by Cs90 (Ag_2O) and Cc90 (Ag_2O) catalysts in 5–30 min and by CD90 (Ag_2O) catalyst in 20–60 min.
- The greater catalytic efficiency of surfactant-containing catalysts (Cs90 (Ag_2O) and Cc90 (Ag_2O)) than non-surfactant catalysts (CD90 (Ag_2O)) is attributed to the specific role of surfactants in providing more solubility, surface area, and reactive centers.
- The kinetics followed by synthesized catalysts in the degradation of 4-NP was first-order and the catalysts have the potential to use in many recycling turns.
- The Cs90 (Ag_2O) and Cc90 (Ag_2O) catalyzed 4-NP 5 times whereas it was degraded 3 times by CD90 (Ag_2O) catalyst.
- This study recommends the use of synthesized catalysts in the industrial process like the lining of the reactor, filter-bed, or flow system.

Acknowledgments

The authors are grateful to the National Center for Physics, Pakistan, for kindly providing MWCNTs. We are thankful to Dr. Muhammad Farooq, UOP Pakistan, and Mr. Bilal Akram, Tsinghua University China, for help in characterizing the samples.

References

[1] K.K. Sadasivuni, S. Rattan, S. Waseem, S.K. Bramhe, S.B. Kondawar, S. Ghosh, P. Mazumdar, Silver Nanoparticles and Its Polymer Nanocomposites-Synthesis, Optimization, Biomedical Usage, and Its Various Applications, K. Sadasivuni, D. Ponnamma, M. Rajan, B. Ahmed, M. Al-Maadeed, Eds., Polymer Nanocomposites in Biomedical Engineering, Lecture Notes in Bioengineering, Springer, Cham, 2019, pp. 331–373.
[2] B. Tylkowski, A. Trojanowska, M. Nowak, L. Marciniak, R. Jastrzab, Applications of silver nanoparticles stabilized and/or immobilized by polymer matrixes, Phys. Sci. Rev., 2 (2017) 1–16, doi: 10.1515/psr-2017-0024.
[3] T. Dayakar, K.V. Rao, J. Park, K.K. Sadasivuni, K.R. Rao, Non-enzymatic biosensing of glucose based on silver nanoparticles synthesized from *Ocimum tenuiflorum* leaf extract and silver nitrate, Mater. Chem. Phys., 216 (2018) 502–507.
[4] T. Kamal, I. Ahmad, S.B. Khan, A.M. Asiri, Bacterial cellulose as support for biopolymer stabilized catalytic cobalt nanoparticles, Int. J. Biol. Macromol., 135 (2019) 1162–1170.
[5] S.Y. Park, J.W. Chung, Y.K. Chae, S.Y. Kwak, Amphiphilic thiol functional linker mediated sustainable anti-biofouling ultrafiltration nanocomposite comprising a silver nanoparticles and poly(vinylidene fluoride) membrane, ACS Appl. Mater. Interfaces, 5 (2013) 10705–10714.
[6] S.Y. Park, J.W. Chung, R.D. Priestley, S.Y. Kwak, Covalent assembly of metal nanoparticles on cellulose fabric and its antimicrobial activity, Cellulose, 19 (2012) 2141–2151.
[7] A. Popelka, P. Sobolciak, M. Mrlík, Z. Nogellova, I. Chodák, M. Ouederni, M.A. Al-Maadeed, I. Krupa, Foamy phase change materials based on linear low-density polyethylene and paraffin wax blends, Emerg. Mater., 1 (2018) 1–8.
[8] F.S. Kodeh, I.M. El-Nahhal, E. Abou Elkhair, A.H. Darwish, Synthesis of CaO-Ag-NPs@$CaCO_3$ nanocomposite via impregnation of aqueous sol Ag-NPs onto calcined calcium oxalate, Chem. Afr., 14 (2019) 1–8.
[9] D.T. Santos, B.F. Sarrouh, J.D. Rivaldi, A. Converti, S.S. Silva, Use of sugarcane bagasse as biomaterial for cell immobilization for xylitol production, J. Food Eng., 86 (2008) 542–548.
[10] Y. Wu, Y. Zhang, J. Zhou, D. Gu, Recent progress on functional mesoporous materials as catalysts in organic synthesis, Emerg. Mater., 3 (2020) 1–20.
[11] D.P. Wagh, G.D. Yadav, Selectivity engineering in catalysis by ruthenium nanoparticles supported on heteropolyacid-encapsulated MOF-5: one-pot synthesis of allyl 4-cyclohexane butyrate and kinetic modeling, Emerg. Mater., 3 (2020) 965–988.
[12] T. Mozammel, D. Dumbre, P.R. Selvakannan, K.K. Sadasivuni, S.K. Bhargava, Calcined hydrotalcites of varying Mg/Al ratios supported Rh catalysts: highly active mesoporous and stable catalysts toward catalytic partial oxidation of methane, Emerg. Mater., 4 (2021) 469–481.
[13] D.P. Stankus, S.E. Lohse, J.E. Hutchison, J.A. Nason, Interactions between natural organic matter and gold nanoparticles stabilized with different organic capping agents, Environ. Sci. Technol., 45 (2011) 3238–3244.
[14] S. Bibi, G.J. Price, T. Yasin, M. Nawaz, Eco-friendly synthesis, and catalytic application of chitosan/gold/carbon nanotube nanocomposite films, RSC Adv., 6 (2016) 60180–60186.
[15] E. Guibal, Heterogeneous catalysis on chitosan-based materials: a review, Prog. Polym. Sci., 30 (2005) 71–109.
[16] H. Huang, X. Yang, Synthesis of chitosan-stabilized gold nanoparticles in the absence/presence of tripolyphosphate, Biomacromolecules, 5 (2004) 2340–2346.
[17] K. Norajit, K.M. Kim, G.H. Ryu, Comparative studies on the characterization and antioxidant properties of biodegradable alginate films containing ginseng extract, J. Food Eng., 98 (2010) 377–384.
[18] A. Bibi, S. Rehman, A. Yasin, Alginate-nanoparticles composites: kinds, reactions and applications, Mater. Res. Express, 6 (2019) 1–15, doi: 10.1088/2053-1591/ab2016.
[19] M.A. Kamal, S. Bibi, S.W. Bokhari, A.H. Siddique, T. Yasin, Synthesis and adsorptive characteristics of novel chitosan/graphene oxide nanocomposite for dye uptake, React. Funct. Polym., 110 (2017) 21–29.
[20] A.M.F. Lima, M.D.F. Lima, O.B.G. Assis, A. Raabe, H.C.D. Amoroso, V.A. Oliveira Tiera, M.J. Tiera, Synthesis and physicochemical characterization of multiwalled carbon nanotubes/hydroxamic alginate nanocomposite scaffolds, J. Nanomater., 2018 (2018) 1–12.
[21] B. Joddar, E. Garcia, A. Casas, C.M. Stewart, Development of functionalized multi-walled carbon-nanotube-based alginate hydrogels for enabling biomimetic technologies, Sci. Rep., 6 (2016) 1–12.
[22] M. Arjmand, K. Chizari, B. Krause, P. Pötschke, U. Sundararaj, Effect of synthesis catalyst on structure of nitrogen-doped carbon nanotubes and electrical conductivity and electromagnetic interference shielding of their polymeric nanocomposites, Carbon, 98 (2016) 358–372.
[23] B. Galindo, A. Benedito, E. Gimenez, V. Compañ, Comparative study between the microwave heating efficiency of carbon nanotubes versus multilayer graphene in polypropylene nanocomposites, Composites, Part B, 98 (2016) 330–338.
[24] X. Wu, C. Lu, Y. Han, Z. Zhou, G. Yuan, X. Zhang, Cellulose nanowhisker modulated 3D hierarchical conductive structure of carbon black/natural rubber nanocomposites for liquid and strain sensing application, Compos. Sci. Technol., 124 (2016) 44–51.
[25] M. Ionita, M.A. Pandele, H. Iovu, Sodium alginate/graphene oxide composite films with enhanced thermal and mechanical properties, Carbohydr. Polym., 94 (2013) 339–344.
[26] U.T. Khatoon, K.V. Rao, J.R. Rao, Y. Aparna, Synthesis and Characterization of Silver Nanoparticles by Chemical Reduction Method, International Conference on Nanoscience, Engineering and Technology (CONSET 2011), Chennai, 2011, pp. 97–99.
[27] C.H. Lee, Y.C. Bae, Effect of surfactants on the swelling behaviors of thermosensitive hydrogels: applicability of the generalized Langmuir isotherm, RSC Adv., 6 (2016) 103811–103821.

[28] A. Gangula, R. Podila, L. Karanam, C. Janardhana, A.M. Rao, Catalytic reduction of 4-nitrophenol using biogenic gold and silver nanoparticles derived from *Breynia rhamnoides*, Langmuir, 27 (2011) 15268–15274.
[29] V.K. Vidhu, D. Philip, Catalytic degradation of organic dyes using biosynthesized silver nanoparticles, Micron, 56 (2014) 54–62.
[30] G. Mie, Contributions to the optics of turbid media, particularly of colloidal metal solutions, Ann. Phys., 25 (1976) 377–445.
[31] Y.G. Sun, Y.N. Xia, Plasmonics: metallic nanostructures and their optical properties, Proc. SPIE Int. Soc. Opt. Eng., 5221 (2003) 170–173.
[32] B.M. Gatehouse, S.E. Livingstone, R.S. Nyholm, The infrared spectra of some simple and complex carbonates, J. Chem. Soc., 636 (1958) 3137–3142, doi: 10.1039/JR9580003137.
[33] T.L. Slager, B.J. Lindgren, A.J. Mallmann, R.G. Greenler, Infrared spectra of the oxides and carbonates of silver, J. Phys. Chem., 76 (1972) 940–943.
[34] G. Pasparakis, N. Bouropoulos, Swelling studies and in vitro release of verapamil from calcium alginate and calcium alginate-chitosan beads, Int. J. Pharm., 323 (2006) 34–42.
[35] G.T. Grant, Biological interactions between polysaccharides and divalent cations: the egg-box model, FEBS Lett., 32 (1973) 195–198.
[36] F.U. Khan, S.B. Khan, T. Kamal, A.M. Asiri, I.U. Khan, K. Akhtar, Novel combination of zero-valent Cu and Ag nanoparticles@ cellulose acetate nanocomposite for the reduction of 4-nitro phenol, Int. J. Biol. Macromol., 102 (2017) 868–877.
[37] F. Ali, S.B. Khan, T. Kamal, Y. Anwar, K.A. Alamry, A.M. Asiri, Anti-bacterial chitosan/zinc phthalocyanine fibers supported metallic and bimetallic nanoparticles for the removal of organic pollutants, Carbohydr. Polym., 173 (2017) 676–689.
[38] N. Ali, T. Kamal, M. Ul-Islam, A. Khan, S.J. Shah, A. Zada, Chitosan-coated cotton cloth supported copper nanoparticles for toxic dye reduction, Int. J. Biol. Macromol., 111 (2018) 832–838.
[39] J. Hedberg, M. Lundin, T. Lowe, E. Blomberg, S. Wold, I.O. Wallinder, Interactions between surfactants and silver nanoparticles of varying charge, J. Colloid Interface Sci., 369 (2012) 193–201.
[40] A. Khalil, N. Ali, A. Khan, A.M. Asiri, T. Kamal, Catalytic potential of cobalt oxide and agar nanocomposite hydrogel for the chemical reduction of organic pollutants, Int. J. Biol. Macromol., 164 (2020) 2922–2930.
[41] M.S.J. Khan, T. Kamal, F. Ali, A.M. Asiri, S.B. Khan, Chitosan-coated polyurethane sponge supported metal nanoparticles for catalytic reduction of organic pollutants, Int. J. Biol. Macromol., 132 (2019) 772–783.
[42] K. Esumi, R. Isono, T. Yoshimura, Preparation of PAMAM and PPI metal (silver, platinum, and palladium) nanocomposites and their catalytic activities for reduction of 4-nitrophenol, Langmuir, 20 (2004) 237–243.
[43] R. Rajesh, E. Sujanthi, S.S. Kumar, R. Venkatesan, Designing versatile heterogeneous catalysts based on Ag and Au nanoparticles decorated on chitosan functionalized graphene oxide, Phys. Chem. Chem. Phys., 17 (2015) 11329–11340.
[44] L. Ai, J. Jing, Catalytic reduction of 4-nitrophenol by silver nanoparticles stabilized on environmentally benign macroscopic biopolymer hydrogel, Bioresour. Technol., 132 (2013) 374–377.
[45] K. Kalantari, A.B.M. Afifi, S. Bayat, K. Shameli, S. Yousefi, N. Mokhtar, A. Kalantari, Heterogeneous catalysis in 4-nitrophenol degradation and antioxidant activities of silver nanoparticles embedded in Tapioca starch, Arabian J. Chem., 12 (2017) 5246–5252.
[46] G. Xiao, Y. Zhao, L. Li, J. O. Pratt, H. Su, T. Tan, Facile synthesis of dispersed Ag nanoparticles on chitosan-TiO2 composites as recyclable nanocatalysts for 4-nitrophenol reduction, Nanotechnology, 29 (2018) 1–9.
[47] A. Verma, D.P. Jaihindh, Y.P. Fu, Photocatalytic 4-nitrophenol degradation and oxygen evolution reaction in CuO/g-C_3N_4 composites prepared by deep eutectic solvent-assisted chlorine doping, Dalton Trans., 48 (2019) 8594–8610.
[48] S. Sandip, P. Anjali, K. Subrata, B. Soumen, T. Pal, Photochemical green synthesis of calcium-alginate-stabilized Ag and Au nanoparticles and their catalytic application to 4-nitrophenol reduction, Langmuir, 26 (2010) 2885–2893.
[49] A. Vanaamudan, M. Sadhu, P. Pamidimukkala, Chitosan-Guar gum blend silver nanoparticle bio nanocomposite with potential for catalytic degradation of dyes and catalytic reduction of nitrophenol, J. Mol. Liq., 271 (2018) 202–208.
[50] K. Sravanthi, D. Ayodhya, P.Y. Swamy, Green synthesis, characterization and catalytic activity of 4-nitrophenol reduction and formation of benzimidazoles using bentonite supported zero valent iron nanoparticles, Mater. Sci. Technol., 2 (2019) 298–307.